Science and Technology of Advanced Materials

ISSN: (Print) (Online) Journal homepage: www.tandfonline.com/journals/tsta20

Enhancement of the thermoelectric figure of merit in the dirac semimetal Cd_3As_2 by band-structure and -filling control

Markus Kriener, Takashi Koretsune, Ryotaro Arita, Yoshinori Tokura & Yasujiro Taguchi

To cite this article: Markus Kriener, Takashi Koretsune, Ryotaro Arita, Yoshinori Tokura & Yasujiro Taguchi (08 Oct 2024): Enhancement of the thermoelectric figure of merit in the dirac semimetal Cd_3As_2 by band-structure and -filling control, Science and Technology of Advanced Materials, DOI: 10.1080/14686996.2024.2412971

To link to this article: https://doi.org/10.1080/14686996.2024.2412971

Accepted author version posted online: 08 Oct 2024.

Publisher: Taylor & Francis & The Author(s). Published by National Institute for Materials Science in partnership with Taylor & Francis Group.

Journal: *Science and Technology of Advanced Materials*

DOI: 10.1080/14686996.2024.2412971

Enhancement of the Thermoelectric Figure of Merit in the Dirac Semimetal Cd_3As_2 by Band-Structure and -Filling Control

Markus Kriener[a], Takashi Koretsune[b], Ryotaro Arita[a,c], Yoshinori Tokura[a,d,e], and Yasujiro Taguchi[a]

[a]RIKEN Center for Emergent Matter Science (CEMS), Wako 351-0198, Japan;
[b]Department of Physics, Tohoku University, Miyagi 980-8578, Japan;
[c]Research Center for Advanced Science and Technology, University of Tokyo, Tokyo 153-8904, Japan;
[d]Department of Applied Physics and Quantum-Phase Electronics Center (QPEC), University of Tokyo, Tokyo 113-8656, Japan;
[e]Tokyo College, University of Tokyo, Tokyo 113-8656, Japan

ARTICLE HISTORY
Compiled September 25, 2024

ABSTRACT

Topological materials attract a considerable research interest because of their characteristic band structure giving rise to various new phenomena in quantum physics. Beside this, they are tempting from a functional materials point of view: Topological materials bear potential for an enhanced thermoelectric efficiency because they possess the required ingredients, such as intermediate carrier concentrations, large mobilities, heavy elements etc. Against this background, this work reports an enhanced thermoelectric performance of the topological Dirac semimetal Cd_3As_2 upon alloying the trivial semiconductor Zn_3As_2. This allows to gain fine-tuned control over both the band filling and the band topology in $Cd_{3-x}Zn_xAs_2$. As a result, the thermoelectric figure of merit exceeds 0.5 around $x = 0.6$ and $x = 1.2$ at elevated temperatures. The former is due to an enhancement of the power factor, while the latter is a consequence of a strong suppression of the thermal conductivity. In addition, in terms of first-principle band structure calculations, the thermopower in this system is theoretically evaluated, which suggests that the topological aspects of the band structure change when traversing $x = 1.2$.

KEYWORDS

thermoelectric materials; figure of merit; band structure engineering; band filling; Dirac semimetal; Cd_3As_2

1. Introduction

The development and exploration of sustainable energy devices is a timely task in materials

design and research. One important issue is that a substantial amount of input energy is transferred into heat and lost irretrievably in many applications. To overcome this, the Seebeck effect offers a solution: It allows to regain electrical energy by conversion from waste heat.

CONTACT Markus Kriener. Email: markus.kriener@riken.jp

To quantify the conversion efficiency of bulk materials, the dimensionless figure of merit is used: $ZT = S^2T / (\rho\kappa)$ with the thermopower S, the resistivity ρ, and the thermal conductivity κ (T denotes the temperature). The goal is to maximize ZT [1–6]. However, the involved quantities ρ, S, and κ are strongly interrelated and difficult to tune independently, which explains why to date only a few materials with somewhat large ZT values were found. Hence, there is a continuing demand on identifying new promising materials which ideally exhibit large ZT values over a wide temperature range.

Various strategies and concepts to enhance ZT have been proposed and employed, such as exploiting strong correlation effects [7, 8], carrier concentration control [9–11], band structure engineering (band convergence and resonance level formation) [4, 5, 11–20], magnetic interactions [21, 22], utilizing physical pressure [23], or nanostructured devices [13, 24, 25]. "Phonon glass + electron crystal" is often referred to as the guiding principle, i.e., a material should possess ideally independent charge- and heat-transport channels to obtain small ρ and κ values simultaneously [3, 26].

Against this background, it is interesting that some materials with promising thermoelectric features have attracted attention from a different point of view in recent years: they were identified to possess a topologically nontrivial band structure, such as the prototypical thermoelectric Bi_2Te_3 [27–29]. The coincidence of topological nontriviality and thermoelectric efficiency is, however, not surprising since both phenomena partly share the same ingredients: intermediate carrier concentrations, large mobilities, heavy elements, or narrow band gaps [30, 31]. This motivated us to focus on the Dirac semimetal Cd_3As_2 [32–39]. Beside its topological features, it has long been known for its large room-temperature mobility of $\sim 10^4 - 10^7$ $cm^2 V^{-1} s^{-1}$ while the electron charge carrier concentration lies at moderate $\sim 10^{18}$ cm^{-3} [34, 40]. Moreover, its thermal conductivity was reported to be as small as 2.5 – 4 $WK^{-1}m^{-1}$ at 300 K with an extremely tiny lattice contribution $\kappa_{ph} \sim 1$ $WK^{-1}m^{-1}$ [41–45]. Consistently, a room-temperature figure of merit $ZT \sim 0.1$ was reported [43, 46], with an additional slight enhancement upon shallow Cr doping [43]. In thin films of Cd_3As_2, enhanced values of the thermopower and the power factor S^2/ρ were reported at low temperatures as a function of the film thickness [47]. There is also theoretical support that topological materials such as Cd_3As_2 are promising playgrounds to look for a reasonable thermoelectric performance [48–50].

Here, we chose to mix the $4d$ system Cd_3As_2 with its lighter $3d$ counterpart Zn_3As_2 because partial Zn doping modifies both the band filling and the band structure: A hole carrier concentration of $\sim 10^{17}$ cm^{-3} and a much smaller mobility of a few 10 $cm^2 V^{-1} s^{-1}$ reported for Zn_3As_2 suggest that alloying offers to fine tune and gain control of these quantities and, hence, the figure of merit of $Cd_{3-x}Zn_xAs_2$ across the charge neutrality point [51–54]. In addition, the question at what x the topological band inversion in Cd_3As_2 switches back to normal band order is tempting since Zn_3As_2 is theoretically a trivial band insulator. Recent reports allocate this change around $x \sim 1.1$ for the bulk system [54] while it was seen at a smaller $x \sim 0.6$ in thin-film studies [55–57].

Figure 1. (a) Schematic of Cd_3As_2 in its tetragonal $P4_2/nmc$ structure ("β-Cd_3As_2"). In

this setting, the characteristic voids (gray shadows) on the Cd sites arrange along the a or b axis, cf. Ref. [33]. Band structures of (b) Cd_3As_2 and (c) Zn_3As_2 based on the structural β modification. In the inset, the band structure of Cd_3As_2 around the Γ point is magnified with the Dirac-like band dispersion highlighted in red.

In a preceding work [58], where we only focussed on the thermoelectric performance of $Cd_{3-x}Zn_xAs_2$ below room temperature in the very limited Zn concentration range $0 \le x \le 1.2$, we reported that ZT reaches $\sim 0.3 \pm 0.1$ for $x \sim 0.8-1.0$. This and the sizable slope of $ZT(T)$ at room temperature motivated the present work, in which we largely extend our previous study to approximately 650 K and target the whole solid solution $0 \le x \le 3$. Moreover, in the present work we also modeled the band structure on the basis of first-principle calculations for Cd_3As_2 and Zn_3As_2, and subsequently calculated the temperature dependence of the thermopower for various carrier concentrations for comparison with the experimental results to give an insight into the question where the topological aspects of the band structure may change.

The examination of this much wider phase space in terms of temperature and Zn concentration allowed to identify two different x ranges where ZT becomes large: At 600 K, ZT exceeds 0.5 around $x \sim 0.6$ and ~ 1.2. In addition, the comparison of theoretical and experimental thermopower data yielded strong support for the conclusion that the topological band order vanishes between $x = 1.0$ and 1.2.

2. Results

We start with a brief discussion of the structure-related situation in $Cd_{3-x}Zn_xAs_2$. At ambient conditions, a series of structural modifications is realized as a function of x. Moreover, for the end compounds Cd_3As_2 and Zn_3As_2, two different modifications are discussed in the literature, referred to as α phase in this work: the body-centered tetragonal space groups $I4_1/acd$ (no. 142) [51, 33] and $I4_1/cd$ (no. 110) [59, 60]. According to a recent publication, the former one seems realized in Cd_3As_2 [33]. In the Zn concentration range $0.6 \le x \le 1.2$, the system crystallizes in the simple tetragonal space group $P4_2/nmc$ (no. 137, β phase) and for $1.5 \le x \le 2.5$ it takes the closely related superstructure $I4_1/amd$ (no. 141; β' phase). This complex situation is discussed in more detail in Section S1 in the accompanying Supplemental Material (SM) [61]. A schematic plot of the β-type crystal structure is shown in Fig. 1(a).

Figures 1(b) and (c) summarize the results of band-structure calculations for the two pristine materials Cd_3As_2 and Zn_3As_2, respectively. These are based on the β phase which was chosen for an easy comparison with experimental data for alloyed samples. For Cd_3As_2 and Zn_3As_2, the main features of the β phase are the same as in the α modifications. Notably, Cd_3As_2 remains a semimetal and exhibits a band crossing with Dirac-like dispersion near the Γ point close to the Fermi energy as can be seen in the magnified inset in Fig. 1. The opposite end compound Zn_3As_2 is a trivial band insulator in both structural modifications, while Zn_3As_2 is conductive due to unintentionally doped holes in reality.

Figure 2. Temperature dependence of the thermoelectric properties of the solid solution $Cd_{3-x}Zn_xAs_2$ ($0 \le x \le 3$): (a) resistivity ρ, (b) thermopower S, (c) power factor S^2/ρ, (d) thermal conductivity κ, and (e) figure of merit $ZT = S^2T/(\rho\kappa)$. In (c) the data for $x = 2.0$ (overall very small S^2/ρ) and in (d) the data for some x are omitted for clarity. The latter can be found in Section S3 in the SM [61].

Figure 2 summarizes the temperature dependence of all quantities related to the figure of merit of $Cd_{3-x}Zn_xAs_2$. The resistivity $\rho(T)$ is shown in Fig. 2(a). Except for the strong increase for $T < \sim 150$ K in the data for $x = 0.8$, all samples with $0.6 \le x \le 1.0$ exhibit a metallic-like temperature dependence up to a temperature T_{max} and then decrease. As a function of x, T_{max} decreases monotonically, suggesting that there is also a maximum outside the targeted temperature range in ρ for $x = 0$, which tends to saturate above 600 K. As for the low-temperature increase in the data of $x = 0.8$, we occasionally observe such metal-insulator transitions below room temperature for $x \le 1.2$, cf. Ref. [58] and Section S7 in the SM [61].

For $x \ge 1.2$, the resistivity of $Cd_{3-x}Zn_xAs_2$ is strongly enhanced and exhibits maxima, which shift up to $x = 2.5$ toward higher temperatures. The data for $x \ge 1.5$ look qualitatively similar while the absolute values of the resistivity increases with x except for Zn_3As_2, in rough agreement with the literature [51]. The maxima imply that additional charge carriers are activated at elevated temperatures, possibly leading to bipolar conduction. In Section S5 in the SM [61], we present an Arrhenius analysis of the high-temperature resistivity.

Figure 2(b) summarizes corresponding thermopower $S(T)$ data. For all samples $x \le 1$, we observe a negative S except at very low temperatures. There are also distinct extrema whose temperatures T_1 decrease monotonically with x. As expected for these metallic samples, S exhibits roughly a linear temperature dependence below T_1 with some deviations for $x = 0.8$ and 1.0 at low temperatures. Above T_1, the absolute value of S decreases. Upon further increasing x, there is a clear qualitative and quantitative change. For $x = 1.2$ and 1.5, S exhibits two extrema at T_1 and T_2 ($< T_1$). In between the sign of S changes from positive to negative. For $T > T_1$, S of these two samples is qualitatively similar to what is observed for $x \le 1$. For $x = 2.0$, there is no sign change of S any more but the two extrema as characteristic features are still visible although $T_1(x)$ has almost shifted out of the examined temperature range. The latter seems to be the case for $x = 2.5$ and 3, each of which exhibits only a broad extremum up to 650 K. The x dependencies of these characteristic temperatures in $\rho(T)$ and $S(T)$ are replotted in Fig. 5.

Corresponding power-factor data $S^2/\rho(T)$ are plotted in Fig. 2(c), which is strongly enhanced over the entire temperature range studied when going from $x = 0$ to 0.6. For $x = 0.8$ and 1.0, S^2/ρ is similar to $x = 0$ up to above room temperature and exceeds it toward 650 K. For $x = 1.2$ and 1.5, S^2/ρ are much smaller than for $x \le 1$ up to above room temperature, reflecting the large resistivities of these samples. Toward 650 K, a steep increase is observed for both and, in the case of $x = 1.2$, it even exceeds $x = 0$. For the sample with $x = 2.0$, S^2/ρ is rather small throughout the examined temperature range [not shown for clarity in Fig. 2(c)]. For

$x = 2.5$ and 3.0, there is a slight increase above ~ 400 K.

Figure 2(d) summarizes thermal conductivity $\kappa(T)$ data. Beside the increases below ~ 100 K, κ of $Cd_{3-x}Zn_xAs_2$ is remarkably small. For $x = 0$, we observe $\kappa < 4$ $WK^{-1}m^{-1}$. Moreover, κ is further suppressed when introducing Zn and takes its minimum for $x = 1.5$ in most of the temperature range. Toward Zn_3As_2, κ increases again but remains below that for $x = 0$.

The figure of merit $ZT(T)$ for all examined samples is shown in Fig. 2(e). For $0 \le x \le 1.0$ we find relatively large ZT values from well below room temperature, which further increase as a function of temperature up to about 500 K. Above, ZT exhibits a maximum or an onset of a maximum. For $x = 1.2$ and 1.5, ZT remains small up to ~ 350 K and 420 K, respectively. Upon further increasing temperature, these two samples also exhibit comparably large ZT values. Interestingly, ZT of $x = 1.2$ eventually exceeds the data of $x = 0.6$, although only above 600 K. For $x = 2.5$ and 3.0, we find slightly enhanced ZT values above ~ 500 K.

3. Discussion

3.1. The Figure of Merit

Figure 3. Zn concentration x dependence of (a) the resistivity ρ, (b) the thermopower S, (c) the power factor S^2/ρ, (d) the charge carrier concentration $|n_H|$ as estimated from field-dependent Hall-resistivity data, and (e) the corresponding charge carrier mobility μ of $Cd_{3-x}Zn_xAs_2$ ($0 \le x \le 3$). Blue (red) symbols indicate data taken at 300 K (600 K). Blueish and reddish bold lines are guides to the eyes, and the gray shaded areas in (d) and (e) indicate the Zn concentration range in which electrons (filled symbols) and holes (open symbols) apparently coexist as charge carriers, see text.

Figures 3 and 4 summarize several important quantities at 300 K and 600 K as a function of the Zn concentration x. In Fig. 3(a), the strong enhancement of the resistivity $\rho(x)$ with x is well recognizable in the 300-K data across $x = 1$. In the 600-K data, this increase is less steep. A consequence of the maxima in $\rho(T)$ is that, except for $x \le 0.6$, the resistivity values at 600 K are smaller than those at 300 K.

Figure 3(b) contains the respective thermopower data $S(x)$. The sign change of S from negative ($x \le 1.0$) to positive ($x \ge 2.0$) is clearly discernible. The occurrence of extrema above 300 K in $S(T)$ leads to comparable absolute values of the thermopower at 300 K and 600 K for $x \le 1.0$ and $x \ge 2.5$. In between, the two extrema in $S(T)$ cause very different values of S at 300 K and 600 K. For $x = 1.5$, S changes from about +600 μVK^{-1} to –300 μVK^{-1}.

These observations are reflected in the power-factor data $S^2/\rho(x)$ shown in Fig. 3(c). The still relatively small resistivity and large absolute thermopower for $x \le 1.0$ manifests itself as a strong enhancement of S^2/ρ with a peak at $x = 0.6$ at both temperatures shown. The recovery of the thermopower for $x \ge 2.5$ results only in a slight increase of S^2/ρ toward Zn_3As_2 due to the large resistivity.

Figures 3(d) and (e) summarize the x dependencies of the absolute values of the charge carrier concentration $|n_{\mathrm{H}}|$ as estimated from magnetic field B-dependent Hall-resistivity measurements $\rho_{yx}(B)$ at 300 K and the corresponding mobility $\mu = 1/(|n_{\mathrm{H}}|\rho e)$ with the elementary charge e, respectively.

Figure 4. Zn concentration x dependence of (a) the thermal conductivity and (b) the dimensionless figure of merit ZT of $Cd_{3-x}Zn_xAs_2$ ($0 \le x \le 3$). Blue (red) symbols denote data taken at 300 K (600 K). Blueish and reddish bold lines are guides to the eyes.

When introducing Zn into the system, the electronic transport remains initially dominated by electrons. Their concentration of $\sim 10^{18}$ cm^{-3} for $x = 0$ is reduced by approximately one order of magnitude for $x = 1.0$, i.e., the band filling (with electrons as charge carriers) is reduced when introducing Zn into Cd_3As_2. Upon further alloying, the drop of the electron concentration is accelerated and falls below 10^{15} cm^{-3} for $x = 1.2$ and 1.5. At the same time, holes with a concentration of 10^{17} – 10^{18} cm^{-3} also start to contribute to the electronic transport, highlighting the change in the nature of the band filling as a function of x. The simultaneous presence of holes and electrons causes strongly non-linear Hall-resistivity data, cf. Figs. S13 and S14 in Section S4 in the SM [61]. The temperature dependence of both carrier types for these two samples can be found therein in Fig. S15. For $x \ge 2.0$, holes are the dominating charge carriers. Their concentration and, hence, the band filling does not change much. A simple phenomenological model of the band-filling evolution fitting to these observations is presented in Section S6 in the SM [61]. Another interesting point here is that the mobility of pristine Cd_3As_2 is apparently smaller than for $x = 0.6$, above which it decreases again as a function of x. We will come back to this feature later.

Importantly, the electrons governing the transport on the Cd-rich side of the phase diagram maintain their large mobility which amounts to several 1000 cm^2 V^{-1} s^{-1} for $x \le 1.2$, cf. Fig. 3(e). By contrast, the hole carriers for all samples $x \ge 1.2$ exhibit low mobility values of less than 70 cm^2 V^{-1} s^{-1}, i.e., Zn alloying removes high-mobility electrons and replaces them with low-mobility holes while the hole concentrations for $x \ge 1.2$ are on a similar order of magnitude as those of the electrons for $x \le 1.0$.

As seen in Fig. 4(a), $Cd_{3-x}Zn_xAs_2$ exhibits an overall small $\kappa(x)$ at both 300 K and 600 K. The values at 300 K are smaller (larger) than those at 600 K for $x \le 1.5$ ($x \ge 2.0$). The largest values of $\kappa \sim 3$ WK^{-1}m^{-1} are found in pure Cd_3As_2 in agreement with previous reports in the literature [41–45]. Upon Zn alloying, κ is further suppressed. We observe the smallest thermal conductivity $\kappa < 1$ WK^{-1}m^{-1} at 300 K for $x = 1.5$ and at 600 K for $x = 2.5$. This additional suppression of κ is due to the vanishing electronic contributions for larger x, as it is discernible in Figs. S10 and S12 in the SM [61].

Figure 4(b) displays the figure of merit $ZT(x)$ of $Cd_{3-x}Zn_xAs_2$. At 300 K, the enhancement of S^2/ρ [Fig. 3(c)] and the suppression of κ [Fig. 4(a)] lead to two peaks in $ZT(x)$. The first peak is observed at $x = 0.6$, for which ZT is close to 0.2. The second peak appears at $x = 1.0$, where ZT reaches ~ 0.15. For $x > 1.0$, ZT is almost negligible because of

the large resistivity values measured for these samples around 300 K.

At 600 K, The first peak is again observed at $x = 0.6$ while the second peak has shifted to $x = 1.2$. In both cases ZT exceeds 0.5. The main driving ingredient in the former case is the power factor, while in the latter case the strong suppression of the thermal conductivity at intermediate x provides the biggest impact. Hence, the drop of ZT across $x = 0.8$ at both temperatures is mainly due to the fading of the power factor in this x range while the thermal conductivity has not yet been reduced sufficiently to compensate for it. For $x > 1.2$, ZT is strongly suppressed at 600 K, taking its lowest value at $x = 2.0$. Upon further increasing x, a slight increase to almost $ZT \sim 0.1$ appears, which is mainly due to an again enhanced thermopower with x at elevated temperatures in combination with the still fairly small thermal conductivity.

Figure 5. Contour plots of all properties relevant to the figure of merit in $Cd_{3-x}Zn_xAs_2$ as a function of the Zn concentration x (horizontal axis) and the temperature T (vertical axis): (a) resistivity ρ, (b) and (c) absolute thermopower $|S|$ for $S < 0$ and $S > 0$, respectively (note the different scale bars), (d) power factor S^2/ρ, (e) thermal conductivity κ, and (f) figure of merit ZT. In panel (a), the maxima in the temperature dependence of the resistivity (T_{max}) and in panels (b) – (f) the respective extrema in temperature-dependent thermopower data (T_1 and T_2) are superimposed. The color code in all panels is chosen so that red and blue indicate advantageous and disadvantageous for enhancing ZT, respectively.

Complementary contour plots are presented in Fig. 5, which allow to easily perceive the overall evolution of the thermoelectric quantities and how they contribute to ZT in $Cd_{3-x}Zn_xAs_2$. The resistivity is shown in Fig. 5(a). Its strong increase up to $x \sim 2.5$ at elevated temperatures and in the whole x range at low temperatures are clearly revealed.

Figures 5(b) and (c) depict the absolute values of the thermopower $|S|$ for $S < 0$ (smaller x) and $S > 0$ (larger x), respectively. The initial increase of $|S|$ with x and T, when starting to introduce Zn, is traceable in Fig. 5(b). The thermopower takes its largest absolute values at intermediate x as indicated by the two red hot spots in the central upper half of Fig. 5(b) and the central lower half of Fig. 5(c), where the shift of T_2 with x toward higher temperatures accompanied by a slow reduction of $|S|$ is well resolved. The contour plot of the power factor S^2/ρ shown in Fig. 5(d) peaks around $x = 0.6$ as functions of x and T, making it apparent how $ZT(x)$ is enhanced at elevated temperatures for $x < \sim 1.2$.

The plot of the thermal conductivity in Fig. 5(e) reveals how κ is suppressed with x and T and that it remains small almost up to $x = 3.0$, where some thermal conductivity is regained. The resulting figure of merit is shown in Fig. 5(f), where the second peak in $ZT(x)$ around $x = 1.2$ and at elevated temperatures is revealed and can be easily traced back to the concomitant suppression of κ.

3.2. Topological Aspects of the Band Structure

Figure 6. Calculated temperature dependence of the thermopower S_{calc} of (a) Cd_3As_2 and (b) Zn_3As_2 for different charge carrier densities [electrons in (a) and holes in (b), respectively] under the assumption of a rigid-band shift of the Fermi level. The change in the carrier count is indicated by the coloring (from large ↔ red to small ↔ blue). This reduction corresponds to the effect of the increase of the Zn (Cd) concentration in the experiment when starting from Cd_3As_2 (Zn_3As_2). The carrier counts are given in (a) in electrons per unit cell (corresponding to approximately 10^{18} cm^{-3}–10^{19} cm^{-3}) and in (b) in holes per unit cell (10^{17} cm^{-3}–10^{19} cm^{-3}; 0.001 per unit cell corresponds to approximately $1\times10^{18}\,cm^{-3}$).

Finally, we discuss whether the anticipated changes in the band structure when alloying the Dirac semimetal Cd_3As_2 with the trivial semiconductor Zn_3As_2 are reflected in our experimental observations shown in Figs. 2 – 4. To this end, we theoretically calculated the thermopower as a function of temperature and for different charge carrier concentrations on the basis of the band structures for Cd_3As_2 and Zn_3As_2, presented in Figs. 1(b) and (c), respectively. These assume the β structural phase $P4_2/nmc$ which is realized for $0.6 \le x \le 1.2$. The β'-phase, which forms for $1.5 \le x \le 2.5$, has a superstructure in which the length of the crystallographic c axis is doubled, cf. Section S1 in the SM [61]. The band structures as well as the band gaps are likely to be similar in both phases and, hence, also the resulting thermopower. Moreover, in the calculations to determine S_{calc} for Zn_3As_2, the band gap was reduced to 50% of its obtained value (0.76 eV) by shifting the conduction bands in order to mimic the band structure for the intermediate region particularly around $1.2 \le x \le 1.5$, where the band gap is expected to be smaller than that of the end compound Zn_3As_2. It should also be noted that we apply the constant-τ (scattering time) approximation while the energy dependence of τ may contribute to S significantly near the anticipated change in the band structure.

Figures 6(a) and 6(b) summarize the temperature dependencies of the calculated thermopower S_{calc} for several charge carrier concentrations for Cd_3As_2 and Zn_3As_2, respectively. The change in the carrier count in the calculations mimics the observed change in the experimental carrier concentration induced by alloying Cd_3As_2 and Zn_3As_2, as shown in Fig. 3(d): Upon partially replacing Cd with Zn, the electron concentration is reduced while the hole concentration decreases upon introducing Cd into Zn_3As_2 toward the intermediate x range.

A comparison of S_{calc} and the experimental results S_{exp} shown in Fig. 2(b) reveals striking similarities: In the case of Cd_3As_2 [Fig. 6(a)], the theoretical curve with the largest electron concentration has to be compared with the experimental data for $x = 0$: It is negative and exhibits an extremum as seen in the experimental thermopower in Fig. 2(b). Upon reducing the carrier count, the absolute values $|S_{calc}|$ increase and the temperature of the extrema decreases, as seen in S_{exp} as a function of x in Fig. 2(b). Hence, there are qualitative and quantitative similarities between theory and experiment for $0 \le x \le 1.0$ when the thermopower is calculated for Cd_3As_2 with a rigid-band assumption.

As for the opposite end compound Zn_3As_2, the theoretical curve with the largest hole

concentration in Fig. 6(b) has to be compared with the experimental data for $x = 3.0$, both of which exhibit a broad extremum. Upon reducing the carrier count, lower-T extrema develop in $S_{calc}(T)$ and the temperatures of the higher-T extrema decrease. Remarkably, the theoretical data for the smallest carrier counts almost perfectly reproduce the experimental results for $x = 1.2$ and 1.5 shown in Fig. 2(b). Moreover, the calculations for Zn_3As_2 do not only produce the order of magnitude of S_{exp} but also the temperature scale fits well. Apparently, these theoretical data on Zn_3As_2 fit qualitatively and quantitatively to the experimental results for $1.2 \leq x \leq 3.0$.

These observations provide hints that the physics in the solid solution $Cd_{3-x}Zn_xAs_2$ for $0 \leq x \leq 1.0$ is likely governed by a band structure of the same type as realized in the Dirac semimetal Cd_3As_2 [Fig. 1(b)], while for $1.2 \leq x \leq 3.0$ it is of the same type as in Zn_3As_2 [Fig. 1(c)], i.e., the expected changes in the band structure take place between $x = 1.0$ and 1.2. Notably, several other properties also exhibit a significant change in this x range. These are summarized and discussed in Section S6 in the SM [61] and therein shown in Fig. S17.

This finding also allows to speculate why the mobility μ shown in Fig. 3(e) features a maximum at small Zn concentrations. The small effective mass m^* for $x \sim 1.0$ – 1.2 with the chemical potential lying near the Dirac point should become larger when the chemical potential is raised upon increasing charge carrier concentration, i.e., decreasing x, cf. Fig. 3(d). Hence, the mobility $\mu \propto \tau / m^*$ with the scattering time τ should decrease. However, experimentally the opposite is initially observed: μ increases upon decreasing x. This can be understood if the intrinsic disorder due to the mixture of Cd and Zn is taken into account (cf. the discussion in Section S7 in the SM): It is reasonable that the reduced disorder enhances τ, overcompensating the expected effect of the effective mass enhancement upon decreasing x. When the disorder gets more and more reduced upon approaching Cd_3As_2, at some x this overcompensation will fade out and μ can be expected to exhibit a maximum, which we observe around $x \sim 0.6$.

We close the discussion with noting that such a strongly temperature-dependent thermopower including sign changes and the appearance of one or two extrema was also reported for $Bi_{1-x}Sb_x$ alloys, cf., e.g., [62, 63]. This alloy is also bridging between semiconducting and semimetallic states and hosts the first experimentally confirmed three-dimensional topological insulator as a function of x [64, 65], showing a qualitative resemblance with the present $Cd_{3-x}Zn_xAs_2$.

4. Conclusion

To gain control over the thermoelectric figure of merit, this work follows the strategy to start with a topologically nontrivial system, here the Dirac semimetal Cd_3As_2, and to alloy it with a trivial band insulator, namely its lighter counterpart Zn_3As_2. Both materials possess very different physical properties (e.g., metal vs. semiconductor, electron- vs. hole-type conduction, high vs. low mobility). Therefore, studying such a solid solution is a promising approach to gain fine-tuned control over the resistivity ρ, the thermopower S, the thermal conductivity κ, and, hence, the figure of merit $ZT = S^2T / (\rho\kappa)$. The present work demonstrates that this approach

has great potential to be successful: At elevated temperatures, the figure of merit of $Cd_{3-x}Zn_xAs_2$ exhibits two different x ranges around $x = 0.6$ and 1.2, where ZT exceeds ~ 0.5. While the first maximum in $ZT(x)$ can be traced back to an enhancement of the power factor, the second maximum is mainly caused by the suppression of the thermal conductivity.

A comparison of experimental and theoretical thermopower data calculated as a function of temperature for various charge carrier concentrations points toward a scenario that the topological band structure present in the Dirac semimetal Cd_3As_2 changes to trivial between $x = 1.0$ and 1.2. This is further supported by the observation that several other properties in this solid solution also exhibit significant changes in this x range. This work underlines that topologically nontrivial systems are not only fascinating because of their intriguing physics, but that it can be also very promising and valuable to probe their thermoelectric performance especially when bridging toward trivial systems by alloying other elements.

5. Methods

Sample growth and characterization

Polycrystalline batches of $Cd_{3-x}Zn_xAs_2$ with $x = 0$, 0.6, 0.8, 1.0, 1.2, 1.5, 2.0, 2.5, and 3.0 were grown by conventional melt growth. For each batch, inside a glove box stoichiometric amounts of the respective elements (shots of Cd: purity 6N, Asahi Chemical Co. LTD.; Zn: 5N, Nilaco Corp.; As: 7N5, Furukawa Co. LTD.) were loaded into carbonized quartz tubes. These were provisionally closed and transferred to a pumping station where they were evacuated and eventually sealed. Then they were composition-dependently fired to be melted for 48 h to 72 h at 950 °C to 1050 °C and eventually slowly cooled back to room temperature. The phase purity of all batches was checked with an in-house powder x-ray diffractometer (XRD, Rigaku). Our results are in qualitative agreement with the structural phase diagram reported in Ref. [52]. A reproduction of this phase diagram is shown in Fig. S1 in the SM [61]. The concentrations x examined in this work are highlighted therein. The results of the XRD measurements are shown in Figs. S2 and S3 along with the lattice constants as a function of x in Fig. S4. Table S1 provides an overview of the different structural phases existing in this solid solution and their relationship.

The chemical composition of all batches was checked with a scanning-electron microscope equipped with an energy-dispersive x-ray analyzer (SEM-EDX, JEOL and Bruker). Resulting images for selected x are shown in Figs. S5 – S7, and the results of the EDX analyses are summarized in Fig. S8 in the SM [61]. Throughout the text the nominal Zn concentration x is used when referring to samples.

Measurements

Various measurements at low and at elevated temperatures are necessary to determine the figure of merit . Some of them require different sample geometries. Therefore, for each x, several samples were cut from the respective as-grown batches.

Low temperature measurements: The measurements of the longitudinal ρ and the Hall resistivity ρ_{yx} were performed by a conventional five-probe method in a commercial cryostat (phyiscal property measurement system PPMS, Quantum Design), employing the standard resistivity option. The analysis of the Hall resistivity is described in detail in Section S4 in the

SM . The thermopower S and the thermal conductivity κ were measured in homebuilt setups fitting into a PPMS. A temperature gradient was applied to the long side of the respective sample and the voltage difference / temperature gradient was measured by commercial thermocouples, cf. Ref. [58].

High temperature measurements: Resistivity and thermopower were measured by employing a commercial apparatus (ZEM-3, Advance Riko) with the samples kept in He atmosphere and held by two Ni electrodes acting simultaneously as current leads. One of them is equipped with a heater to apply a temperature gradient. Two thermocouples acted as voltage pads in the resistivity measurements and were used to monitor the temperature gradient during the subsequent thermopower measurements. They were mechanically pushed onto a polished sample surface. The same samples used for the high-temperature ρ and S measurements were also used for the respective measurements at low temperatures, which were performed after the high-temperature experience.

The thermal conductivity above room temperature was calculated via $\kappa = \lambda c_p d$ with the thermal diffusivity λ, the specific heat c_p , and the sample density at room temperature d as estimated from the XRD data taken on each batch. To ensure that the XRD density is reliable, we roughly crosschecked it by also estimating the density of each sample from its mass and volume (from the linear dimensions). These two densities agree within ±3 %. The thermal diffusivity was measured in N_2 atmosphere by employing the laser-flash method in a commercial system (LFA-457, Netzsch). For this purpose, the polished top and bottom surfaces of the samples were coated with graphite spray. The specific heat was measured in Ar atmosphere in a commercial system by means of differential scanning calorimetry (STA449 F1 Jupiter, Netzsch).

The misfits between the low- and high-temperature data around room temperature are within 9.5% (resistivity), 8.5% (thermopower), and 15% (thermal conductivity).

We note that the upper limit of the temperature range studied here is due to the decomposition or degradation of $Cd_{3-x}Zn_xAs_2$ at elevated temperatures, as also reported earlier [66, 67]. The exact temperature range where the system dissociates differs between different studies. Our own analyses on powder samples suggest that a detectable mass loss sets in above 650 K.

Comments concerning the known issues about the reproducibility of transport data in Cd_3As_2 (see, e.g., Refs. [34, 68]) and the comparison of the present work with our preceding study [58] can be found in Section S7 in the SM [61]. We note for clarity that all batches were newly grown and that no data published in our previous study [58] are used in the present work while the examined temperature and Zn concentration ranges are largely extended.

Computational Details

Electronic structure calculations were performed in the space group $P4_2/nmc$ with the reported lattice constants for Cd_3As_2 [69] and Zn_3As_2 [70] by using the Vienna Ab initio Simulation Package (VASP) [71]. For Cd_3As_2 , the projector-augmented wave (PAW) method [72, 73] was employed with the exchange correlation functionals of the Perdew-Burke-Ernzerhof (PBE) type [74] in agreement with a previous calculation [32] and for Zn_3As_2 the modified Becke-Johnson (mBJ) type [75, 76], respectively. By using mBJ, we obtain a band gap of 0.76 eV for Zn_3As_2 , which is basically consistent with previous calculations [77, 78]. Spin-orbit coupling

is included in all the calculations using VASP. We utilized the BoltzWann module [79] of the Wannier90 package [80] to calculate the thermopower using a k-point mesh of 100×100×100 and employ the constant-τ approximation, i.e., the energy dependence of the scattering rate is neglected for simplicity.

Acknowledgements

MK acknowledges fruitful discussions with and support by H. Kobayashi (Netzsch Japan), J. Hanss (Netzsch Germany), and D. Maryenko.

Disclosure statement

The authors have no competing interests.

Funding

This work was partly supported by the Japan Society for the Promotion of Science (JSPS, No. 24224009, 15K05140, 19H05825, 22K03447, 22K18954, and 21H01003).

References

[1] Rowe DM. Thermoelectric power generation. Proc IEE. 1978;125:1113. Available from: http://dx.doi.org/doi:10.1049/piee.1978.0247 .

[2] Mahan GD. Good Thermoelectrics. Solid-State Phys. 1997;51:81. Available from: http://dx.doi.org/doi:10.1016/S0081-1947(08)60190-3 .

[3] Snyder GJ, Toberer ES. Complex thermoelectric materials. Nat Mater. 2008;7:105. Available from: https://doi.org/10.1038/nmat2090 .

[4] Pei Y, Shi X, LaLonde A, et al. Convergence of electronic bands for high performance bulk thermoelectrics. Nature (London). 2011;473:66. Available from: http://dx.doi.org/doi:10.1038/nature09996 .

[5] Heremans JP, Wiendlocha B, Chamoire AM. Resonant levels in bulk thermoelectric semiconductors. Energy Environ Sci. 2012;5:5510. Available from: https://doi.org/10.1039/c1ee02612g .

[6] Jarman JT, Khalil EE, Khalaf E. Energy Analyses of Thermoelectric Renewable Energy Sources. Open Journal of Energy Efficiency. 2013;2:37347. Available from: http://dx.doi.org/doi:10.4236/ojee.2013.24019 .

[7] Terasaki I, Sasago Y, Uchinokura K. Large thermoelectric power in $NaCo_2O_4$ single crystals. Phys Rev B. 1997;56:R12685. Available from: https://doi.org/10.1103/PhysRevB.56.R12685 .

[8] Berggold K, Kriener M, Zobel C, et al. Thermal Conductivity, thermopower, and figure of merit of $La_{1-x}Sr_xCoO_3$. Phys Rev B. 2005;72:155116. Available from:

http://dx.doi.org/doi:10.1103/PhysRevB.72.155116 .

[9] Konstantinov PP, Shelimova LE, Avilov ES, et al. Thermoelectric Properties of nGeTe · $m$$Sb_2Te_3$ Layered Compounds. Inorg Mater. 2001;37:662. Available from: http://dx.doi.org/doi:10.1023/A:1017613804472 .

[10] Shimano S, Tokura Y, Taguchi Y. Carrier density control and enhanced thermoelectric performance of Bi and Cu co-doped GeTe. APL Mater. 2017;5:056103. Available from: http://dx.doi.org/10.1063/1.4983404 .

[11] Doi A, Shimano S, Inoue D, et al. Band engineering, carrier density control, and enhanced thermoelectric performance in multi-doped SnTe. APL Mater. 2019;7:091107. Available from: https://doi.org/10.1063/1.5116882 .

[12] Pei Y, LaLonde AD, Wang H, et al. Low effective mass leading to high thermoelectric performance. Energy Environ Sci. 2012;5:7963. Available from: http://dx.doi.org/doi:10.1039/c2ee21536e .

[13] Zhang Q, Liao B, Lan Y, et al. High thermoelectric performance by resonant dopant indium in nanostructured SnTe. Proc Nat Acad Sci. 2013;110:13261. Available from: http://dx.doi.org/doi:10.1073/pnas.1305735110 .

[14] Kriener M, Kikkawa A, Suzuki T, et al. Modification of electronic structure and thermoelectric properties of hole-doped tungsten dichalcogenides. Phys Rev B. 2015;91:075205. Available from: http://dx.doi.org/doi:10.1103/PhysRevB.91.075205 .

[15] Tan G, Shi F, Hao S, et al. Valence Band Modification and High Thermoelectric Performance in SnTe Heavily Alloyed with MnTe. J Am Chem Soc. 2015;137:11507. Available from: http://dx.doi.org/doi:10.1021/jacs.5b07284 .

[16] Wu L, Li X, Wang S, et al. Resonant level-induced high thermoelectric response in Indium-doped GeTe. NPG Asia Mater. 2017;9:e343. Available from: http://dx.doi.org/doi:10.1038/am.2016.203 .

[17] Lee KH, Kim SI, Kim HS, et al. Band Convergence in Thermoelectric Materials: Theoretical Background and Consideration on Bi-Sb-Te Alloys. Adv Energy Mater. 2020;3:2214. Available from: https://doi.org/10.1021/acsaem.9b02131 .

[18] Li F, Liu X, Li SR, et al. Rare three-valence-band convergence leading to ultrahigh thermoelectric performance in all-scale hierarchical cubic SnTe. Energy Environ Sci. 2024;17:158. Available from: https://doi.org/10.1039/d3ee02482b .

[19] Shi X, Song S, Gao G, et al. Global band convergence design for high-performance thermoelectric power generation in Zintls. Science. 2024;384:757. Available from: https://doi.org/10.1126/science.adn7265 .

[20] Gong Y, Dou W, Lu B, et al. Divacancy and resonance level enables high thermoelectric performance in *n*-type SnSe polycrystals. Nat Commun. 2024;15:4231. Available from: https://doi.org/10.1038/s41467-024-48635-0 .

[21] Tsujii N, Nishide A, Hayakawa J, et al. Observation of enhanced thermopower due to spin fluctuation in weak itinerant ferromagnet. Sci Adv. 2019;5:eaat5935. Available from: https://doi.org/10.1126/sciadv.aat5935 .

[22] Vaney JB, Yamini SA, Takaki H, et al. Magnetism-mediated thermoelectric performance of the Cr-doped bismuth telluride tetradymite. Mater Today Phys. 2019;9:100090. Available from: https://doi.org/10.1016/j.mtphys.2019.03.004 .

[23] Nishimura T, Sakai H, Mori H, et al. Large Enhancement of Thermoelectric Efficiency Due to a Pressure-Induced Lifshitz Transition in SnSe. Phys Rev Lett. 2019;122:226601. Available from: https://doi.org/10.1103/PhysRevLett.122.226601 .

[24] Poudel B, Hao Q, Ma Y, et al. High-Thermoelectric Performance of Nanostructured Bismuth Antimony Telluride Bulk Alloys. Science. 2008;320:634. Available from: http://dx.doi.org/doi:10.1126/science.1156446 .

[25] Biswas K, He J, Blum ID, et al. High-performance bulk thermoelectrics with all-scale hierarchical architectures. Nature (London). 2012;489:414. Available from: http://dx.doi.org/doi:10.1038/nature11439 .

[26] Rowe DM, editor. Crc handbook of thermoelectrics. CRC Press, Boca Raton, FL; 1995.

[27] Müchler L, Casper F, Yan B, et al. Topological insulators and thermoelectric materials. Phys Status Solidi RRL. 2013;7:91. Available from: http://dx.doi.org/doi:10.1002/pssr.201206411 .

[28] Ando Y, Fu L. Topological Crystalline Insulators and Topological Superconductors: From Concepts to Materials. Ann Rev Cond Matter Phys. 2015;6:361. Available from: http://dx.doi.org/doi:10.1146/annurev-conmatphys-031214-014501 .

[29] Bansil A, Lin H, Das T. Colloquium: Topological band theory. Rev Mod Phys. 2016;88:021004. Available from: http://dx.doi.org/doi:10.1103/RevModPhys.88.021004 .

[30] Takahashi R, Murakami S. Thermoelectric transport in perfectly conducting channels in quantum spin Hall systems. Phys Rev B. 2010;81:161302(R). Available from: http://dx.doi.org/doi:10.1103/PhysRevB.81.161302 .

[31] Ghaemi P, Mong RSK, Moore JE. In-Plane Transport and Enhanced Thermoelectric Performance in Thin Films of the Topological Insulators Bi_2Te_3 and Bi_2Se_3. Phys Rev Lett. 2010;105:166603. Available from: http://dx.doi.org/doi:10.1103/PhysRevLett.105.166603 .

[32] Wang Z, Weng H, Wu Q, et al. Three-dimensional Dirac semimetal and quantum transport in Cd_3As_2. Phys Rev B. 2013;88:125427. Available from: https://doi.org/10.1103/PhysRevB.88.125427 .

[33] Ali MN, Gibson Q, Jeon S, et al. The Crystal and Electronic Structures of Cd_3As_2, the Three-Dimensional Electronic Analogue of Graphene. Inorg Chem. 2014;53:4062. Available from: https://dx.doi.org/10.1021/ic403163d .

[34] Liang T, Gibson Q, Ali MN, et al. Ultrahigh mobility and giant magnetoresistance in the Dirac semimetal Cd_3As_2. Nat Mater. 2014;14:280. Available from: https://doi.org/10.1038/nmat4143 .

[35] Liu ZK, Jiang J, Zhou B, et al. A stable three-dimensional topological Dirac semimetal Cd_3As_2. Nat Mater. 2014;13:677. Available from: http://dx.doi.org/doi:10.1038/NMAT3990 .

[36] Jeon S, Zhou BB, Gyenis A, et al. Landau quantization and quasiparticle interference in the three-dimensional Dirac semimetal Cd_3As_2. Nat Mater. 2014;13:851. Available from: http://dx.doi.org/doi:10.1038/NMAT4023 .

[37] Uchida M, Nakazawa Y, Nishihaya S, et al. Quantum Hall states in thin films of Dirac semimetal Cd_3As_2. Nat Commun. 2017;8:2274. Available from: https://doi.org/10.1038/s41467-017-02423-1 .

[38] Nakazawa Y, Uchida M, Nishihaya S, et al. Structural characterisation of high-mobility Cd_3As_2 films crystallised on $SrTiO_3$. Sci Rep. 2018;8:2244. Available from: https://doi.org/10.1038/s41598-018-20758-7 .

[39] Uchida M, Koretsune T, Sato S, et al. Ferromagnetic state above room temperature in a proximitized topological Dirac semimetal. Phys Rev B. 2019;100:245148. Available from: http://dx.doi.org/10.1103/PhysRevB.100.245148 .

[40] Turner WJ, Fischler AS, Reese WE. Physical Properties of Several II—V Semiconductors. Phys Rev. 1961;121:759. Available from: https://doi.org/10.1103/PhysRev.121.759 .

[41] Spitzer DP, Castellion GA, GHaacke. Anomalous Thermal Conductivity of Cd_3As_2 and the Cd_3As_2 – Zn_3As_2 Alloys. J Appl Phys. 1966;37:3795. Available from: https://doi.org/10.1063/1.1707927 .

[42] Armitage D, Goldsmid HJ. The thermal conductivity of cadmium arsenide. J Phys C: Solid State Phys. 1969;2:2138. Available from: http://dx.doi.org/doi:10.1088/0022-3719/2/11/328 .

[43] Zhang C, Zhou T, Liang S, et al. Unexpected low thermal conductivity and large power factor in Dirac semimetal Cd_3As_2. Chin Phys B. 2016;25:017202. Available from:

https://doi.org/10.1088/1674-1056/25/1/017202 .

[44] Pariaria A, Khan N, Mandal P. Three-dimensional Dirac semimetal Cd_3As_2 as a potential candidate for thermoelectric applications. Adv Mater AIP Conf Proc. 2018;2005:070005. Available from: https://doi.org/10.1063/1.5050762 .

[45] Yue S, Chorsi HT, Goyal M, et al. Soft phonons and ultralow lattice thermal conductivity in the Dirac semimetal Cd_3As_2. Phys Rev Research. 2019;1:033101. Available from: https://doi.org/10.1103/PhysRevResearch.1.033101 .

[46] Wang H, Luo X, Peng K, et al. Magnetic Field-Enhanced Thermoelectric Performance in Dirac Semimetal Cd_3As_2 Crystals with Different Carrier Concentrations. Adv Func Mater. 2019;29:1902437. Available from: https://doi.org/10.1002/adfm.201902437 .

[47] Ouyang W, Lygo AC, Chen Y, et al. Extraordinary Thermoelectric Properties of Topological Surface States in Quantum-Confined Cd_3As_2 Thin Films. Adv Mater. 2024;36:2311644. Available from: https://doi.org/10.1002/adma.202311644 .

[48] Shi H, Parker D, Du MH, et al. Connecting Thermoelectric Performance and Topological-Insulator Behavior: Bi_2Te_3 and Bi_2Te_2Se from First Principles. Phys Rev Appl. 2015;3:014004. Available from: https://doi.org/10.1103/PhysRevApplied.3.014004 .

[49] Zhou T, Zhang C, Zhang H, et al. Enhanced thermoelectric properties of the Dirac semimetal Cd_3As_2. Inorg Chem Front. 2016;3:1637. Available from: https://doi.org/10.1039/c6qi00383d .

[50] Amarnath R, Bhargavi KS, Kubakaddi SS. Thermoelectric transport properties in 3D Dirac semimetal Cd_3As_2. J Phys: Condens Matter. 2020;32:225704. Available from: https://doi.org/10.1088/1361-648X/ab720f .

[51] Żdanowicz L, Żdanowicz W. Semiconducting Properties of $Cd_{3-x}Zn_xAs_2$-Type Solid Solutions. Phys Solid State. 1964;6:227. Available from: https://doi.org/10.1002/pssb.19640060121 .

[52] Żdanowicz W, Lukaszewicz K, Trzebiatowski W. Crystal Structure of the Semiconducting System Cd_3As_2 – Zn_3As_2. Bull Acad Pol Sci. 1964;12:169.

[53] Żdanowicz W, Żdanowicz L. Semiconducting compounds of the $A^{II}B^{V}$ group. Annual Rev Mater Sci. 1975;5:301. Available from: https://doi.org/10.1146/annurev.ms.05.080175.001505 .

[54] Lu H, Zhang X, Bian Y, et al. Topological Phase Transition in Single Crystals of $(Cd_{1-x}Zn_x)_3As_2$. Sci Rep. 2017;7:3148. Available from: https://doi.org/10.1038/s41598-017-03559-2 .

[55] Nishihaya S, Uchida M, Nakazawa Y, et al. Gate-tuned quantum Hall states in

Dirac semimetal $(Cd_{1-x}Zn_x)_3As_2$. Sci Adv. 2018;4:eaar5668. Available from: http://dx.doi.org/10.1126/sciadv.aar5668 .

[56] Nishihaya S, Uchida M, Nakazawa Y, et al. Negative magnetoresistance suppressed through a topological phase transition in $(Cd_{1-x}Znx)_3As_2$ thin films. Phys Rev B. 2018;97:245103. Available from: https://doi.org/10.1103/PhysRevB.97.245103 .

[57] Nishihaya S, Uchida M, Nakazawa Y, et al. Quantized surface transport in topological Dirac semimetal films. Nat Commun. 2019;10:2564. Available from: http://dx.doi.org/10.1038/s41467-019-10499-0 .

[58] Fujioka J, Kriener M, Hashizume D, et al. Alloying-induced enhancement of thermopower in the Dirac-semimetal system $Cd_{3-x}Zn_xAs_2$. Phys Rev Mater. 2021;5:094201. Available from: http://dx.doi.org/10.1103/PhysRevMaterials.5.094201 .

[59] Steigmann GA, Goodyear J. The Crystal Structure of Cd_3As_2. Acta Cryst B. 1968;24:1062. Available from: https://doi.org/10.1107/S0567740868003705 .

[60] Pietraszko A, Lukaszewicz K. The Crystal Structure of Zinc Arsenide Polymorphic Modifications α-Zn_3As_2 and α'-Zn_3As_2. Bull Acad Pol Sci. 1976;24:459.

[61] See Supplemental Material at [URL will be inserted by publisher] for complementing data.

[62] Ibrahim AM, Thompson DA. Thermoelectric properties of BiSb alloys. Mater Chem Phys. 1985;12:29. Available from: https://doi.org/10.1016/0254-0584(85)90034-3 .

[63] Lenoir B, Dauscher A, Cassart M, et al. Effect of antimony content on the thermoelectric figure of merit of $Bi_{1-x}Sb_x$ alloys. J Phys Chem Solids. 1998;59:129. Available from: https://doi.org/10.1016/S0022-3697(97)00187-X .

[64] Hsieh D, Qian D, Wray L, et al. A topological Dirac insulator in a quantum spin Hall phase. Nature (London). 2008;452:970. Available from: http://dx.doi.org/doi:10.1038/nature06843 .

[65] Ando Y. Topological Insulator Materials. J Phys Soc Jpn. 2013;82:102001. Available from: http://dx.doi.org/doi:10.7566/JPSJ.82.102001 .

[66] Westmore JB, Mann KH, Tickner AW. Mass Spectrometric Study of the Nonstoichiometric Vaporization of Cadmium Arsenide. J Phys Chem. 1964;68:606. Available from: https://doi.org/10.1021/j100785a028 .

[67] Pietraszko A, Lukaszewicz K. Thermal Expansion and Phase Transitions of Cd_3As_2 and Zn_3As_2. Phys Status Solidi A. 1973;18:723. Available from: https://doi.org/10.1002/pssa.2210180234 .

[68] Crassee I, Martino E, Homes CC, et al. Nonuniform carrier density in Cd_3As_2 evidenced by optical spectroscopy. Phys Rev Lett. 2018;97:125204. Available from: http://dx.doi.org/10.1103/PhysRevB.97.125204 .

[69] Pietraszko A, Lukaszewicz K. A refinement of the crystal structure of α''-Cd_3As_2. Acta Cryst B. 1969;25:988. Available from: https://doi.org/10.1107/S0567740869003323 .

[70] Żdanowicz W, Królicki F, Plenkiewicz P. Preparation and semiconducting properties of pseudobinary solid solutions Zn_3As_2-Zn_3P_2. Acta Phys Pol A. 1973;44:447.

[71] Kresse G, Furthmüller J. Efficient iterative schemes for *ab initio* total-energy calculations using a plane-wave basis set. Phys Rev B. 1996;54:11169. Available from: https://doi.org/10.1103/PhysRevB.54.11169 .

[72] Blöchl PE, Jepsen O, KAndersen O. Improved tetrahedron method for Brillouin-zone integrations. Phys Rev B. 1994;49:16223. Available from: https://doi.org/10.1103/PhysRevB.49.16223 .

[73] Kresse G, Joubert D. From ultrasoft pseudopotentials to the projector augmented-wave method. Phys Rev B. 1999;59:1758. Available from: https://doi.org/10.1103/PhysRevB.59.1758 .

[74] Perdew JP, Burke K, Ernzerhof M. Generalized Gradient Approximation Made Simple. Phys Rev Lett. 1996;77:3865. Available from: http://dx.doi.org/doi:10.1103/PhysRevLett.77.3865 .

[75] Becke AD, Johnson ER. A simple effective potential for exchange. J Phys C: Solid State Phys. 2006;124:221101. Available from: https://doi.org/10.1063/1.2213970 .

[76] Tran F, Blaha P. Accurate Band Gaps of Semiconductors and Insulators with a Semilocal Exchange-Correlation Potential. Phys Rev Lett. 2009;102:226401. Available from: https://doi.org/10.1103/PhysRevLett.102.226401 .

[77] Ullah M, Murtaza G, Yaseen M, et al. Band structure features, chemical bonding and optical properties of Zn_3X_2 (X = N, P, As) compounds. J of Alloys and Compounds. 2017;728:1226. Available from: https://doi.org/10.1016/j.jallcom.2017.09.100 .

[78] Hnuna L, Haidar EA, Djamel B, et al. First-principles study of optical and thermoelectric properties of Zn_3As_2 and ZnSb. Nano select. 2023;4:551. Available from: https://doi.org/10.1002/nano.202300074 .

[79] Pizzi G, Volja D, Kozinsky B, et al. BoltzWann: A code for the evaluation of thermoelectric and electronic transport properties with a maximally-localized Wannier functions basis. Comput Phys Commun. 2014;185:422. Available from: http://dx.doi.org/10.1016/j.cpc.2013.09.015 .

[80] Pizzi G, Vitale V, Arita R, et al. Wannier90 as a community code: new features and applications. J Phys: Condens Matter. 2020;32:165902. Available from: http://dx.doi.org/10.1088/1361-648X/ab51ff .

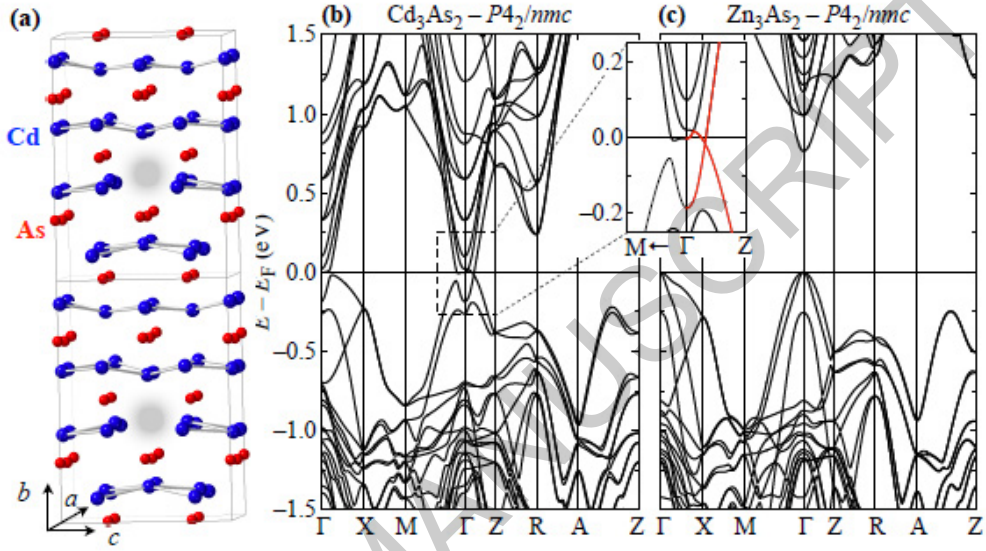

Figure 1. (a) Schematic of Cd_3As_2 in its tetragonal $P4_2/nmc$ structure ("β-Cd_3As_2"). In this setting, the characteristic voids (gray shadows) on the Cd sites arrange along the a or b axis, cf. Ref. [33]. Band structures of (b) Cd_3As_2 and (c) Zn_3As_2 based on the structural β modification. In the inset, the band structure of Cd_3As_2 around the Γ point is magnified with the Dirac-like band dispersion highlighted in red.

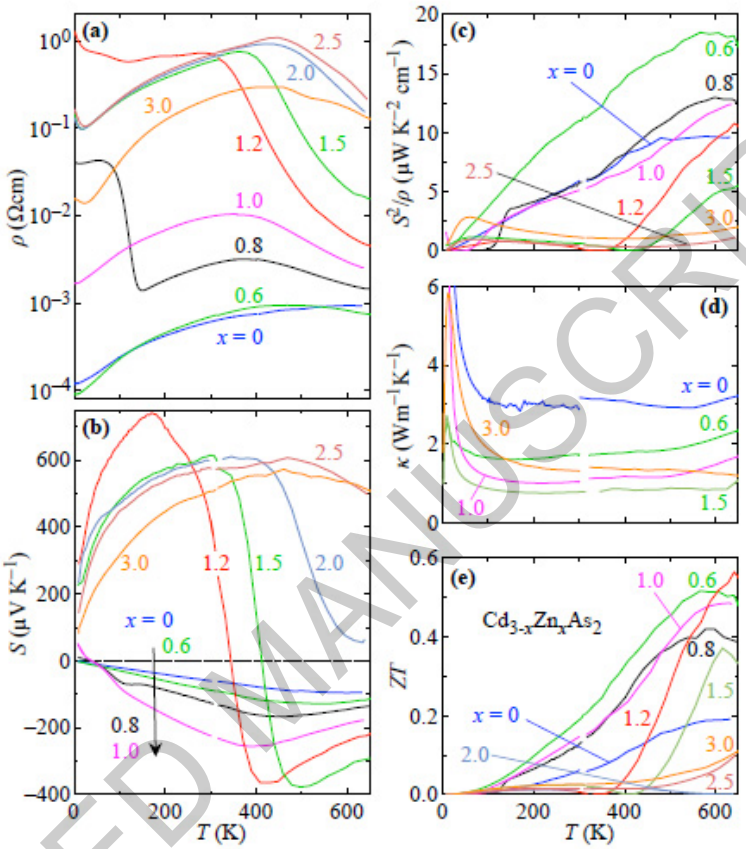

Figure 2. Temperature dependence of the thermoelectric properties of the solid solution $Cd_{3-x}Zn_xAs_2$ ($0 \leq x \leq 3$): (a) resistivity ρ, (b) thermopower S, (c) power factor S^2/ρ, (d) thermal conductivity κ, and (e) figure of merit $ZT = S^2T/(\rho\kappa)$. In (c) the data for $x = 2.0$ (overall very small S^2/ρ) and in (d) the data for some x are omitted for clarity. The latter can be found in Section S3 in the SM [61].

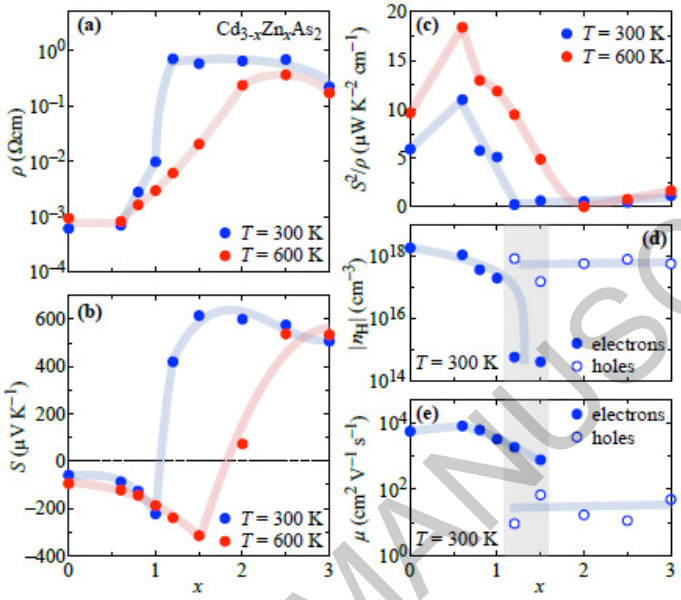

Figure 3. Zn concentration x dependence of (a) the resistivity ρ, (b) the thermopower S, (c) the power factor S^2/ρ, (d) the charge carrier concentration $|n_H|$ as estimated from field-dependent Hall-resistivity data, and (e) the corresponding charge carrier mobility μ of $Cd_{3-x}Zn_xAs_2$ ($0 \leq x \leq 3$). Blue (red) symbols indicate data taken at 300 K (600 K). Blueish and reddish bold lines are guides to the eyes, and the gray shaded areas in (d) and (e) indicate the Zn concentration range in which electrons (filled symbols) and holes (open symbols) apparently coexist as charge carriers, see text.

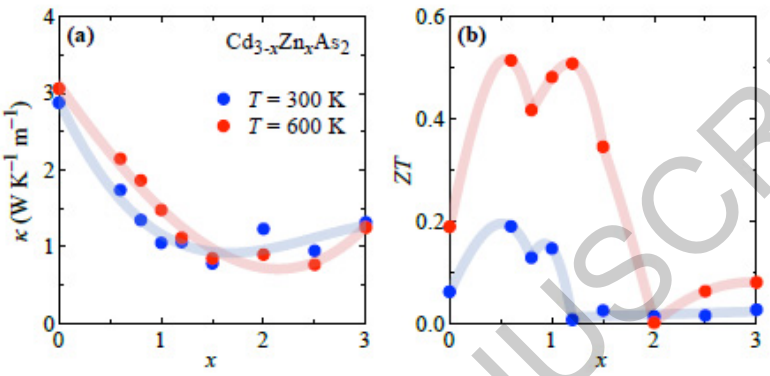

Figure 4. Zn concentration x dependence of (a) the thermal conductivity and (b) the dimensionless figure of merit ZT of $Cd_{3-x}Zn_xAs_2$ ($0 \leq x \leq 3$). Blue (red) symbols denote data taken at 300 K (600 K). Blueish and reddish bold lines are guides to the eyes.

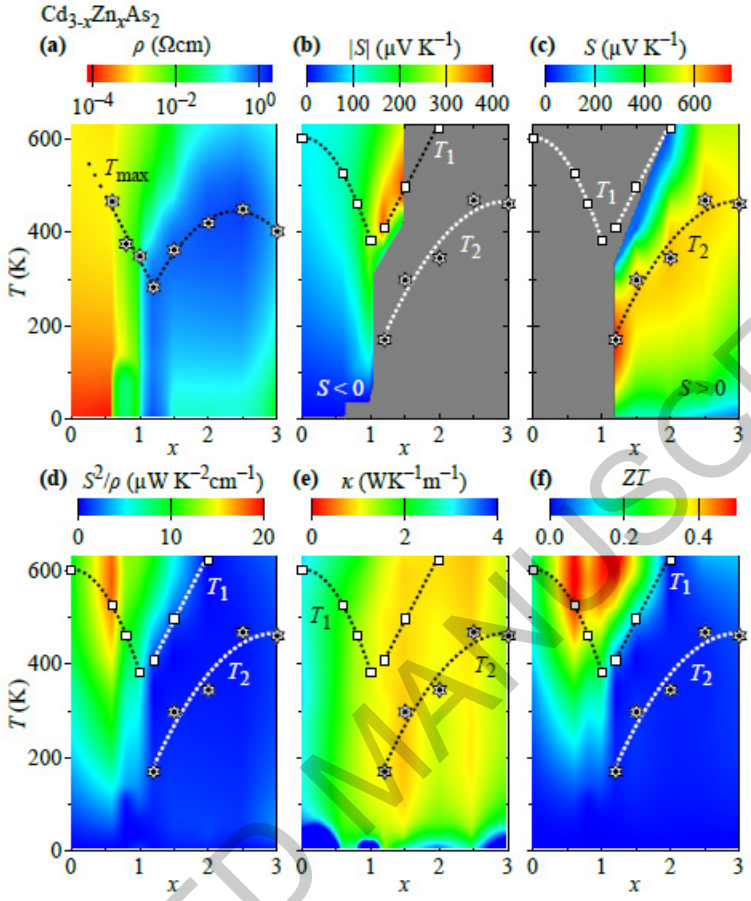

Figure 5. Contour plots of all properties relevant to the figure of merit in $Cd_{3-x}Zn_xAs_2$ as a function of the Zn concentration x (horizontal axis) and the temperature T (vertical axis): (a) resistivity ρ, (b) and (c) absolute thermopower $|S|$ for $S < 0$ and $S > 0$, respectively (note the different scale bars), (d) power factor S^2/ρ, (e) thermal conductivity κ, and (f) figure of merit ZT. In panel (a), the maxima in the temperature dependence of the resistivity (T_{max}) and in panels (b) – (f) the respective extrema in temperature-dependent thermopower data (T_1 and T_2) are superimposed. The color code in all panels is chosen so that red and blue indicate advantageous and disadvantageous for enhancing ZT, respectively.

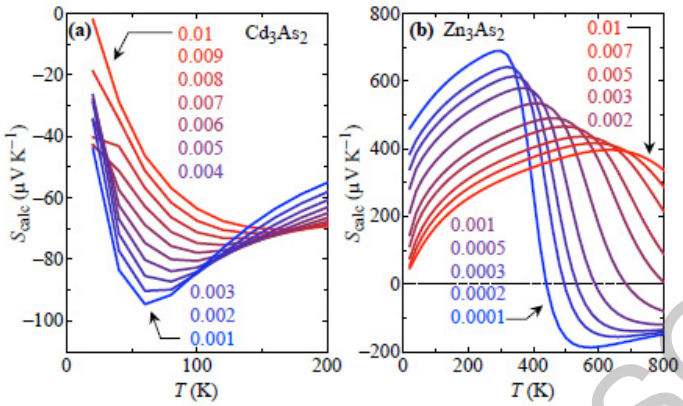

Figure 6. Calculated temperature dependence of the thermopower S_{calc} of (a) Cd_3As_2 and (b) Zn_3As_2 for different charge carrier densities [electrons in (a) and holes in (b), respectively] under the assumption of a rigid-band shift of the Fermi level. The change in the carrier count is indicated by the coloring (from large ↔ red to small ↔ blue). This reduction corresponds to the effect of the increase of the Zn (Cd) concentration in the experiment when starting from Cd_3As_2 (Zn_3As_2). The carrier counts are given in (a) in electrons per unit cell (corresponding to approximately 10^{18} cm^{-3} – 10^{19} cm^{-3}) and in (b) in holes per unit cell (10^{17} cm^{-3} – 10^{19} cm^{-3}; 0.001 per unit cell corresponds to approximately 1×10^{18}cm^{-3}).

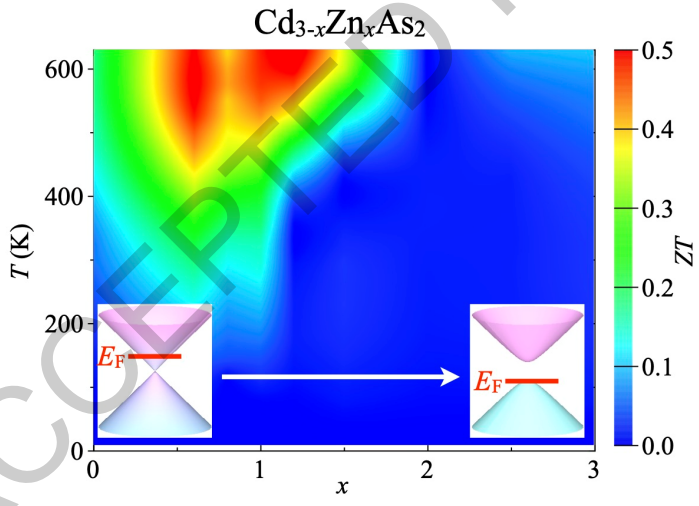

Graphical abstract